Applied Surface Science 552 (2021) 149500

Contents lists available at ScienceDirect

Applied Surface Science

journal homepage: www.elsevier.com/locate/apsusc

Full Length Article

Robust nanotransfer printing by imidization-induced interlocking

Yongrok Jeong [a], Hyeok-jung Kang [a], Zhi-jun Zhao [a], Junseong Ahn [a,b], Soon Hyoung Hwang [a], Sohee Jeon [a], Jiwoo Ko [a,b], Joo-Yun Jung [a], Inkyu Park [b,*], Jun-ho Jeong [a,*]

[a] Korea Institute of Machinery and Materials (KIMM), 156, Gajeongbuk-ro, Yuseong-gu, Daejeon 34103, Republic of Korea
[b] Korea Advanced Institute of Science and Technology (KAIST), 291, Daehak-ro, Yuseong-gu, Daejeon 34141, Republic of Korea

ARTICLE INFO

Keywords:
Nanotransfer printing
Imidization
Mechanical interlocking
Interfacial adhesion
Film heater
Optical blind

ABSTRACT

The importance of the nanotransfer technique has been increased owing to its possibility in nanoscale mass-production, enabled by cost-effective and simply fabricable features. In this study, we developed a novel method for robust nanotransfer printing based on imidization-induced mechanical interlocking. The proposed imidization-induced nanotransfer printing (InTP) method enables various metal nanostructures to be easily transferred onto a polyimide substrate based on the mechanical interlocking force by using a controlled imidization process. The designed functional nanopatterns are transferred with high robustness. In addition, using a partial imidization process, we apply an additional adhesion force at the pattern-substrate interface to transfer materials with poor intrinsic adhesion, such as nickel, successfully. Owing to the exceptional robustness of the method, various 3D nanostructures, such as asymmetric sidewalls, suspended nanowires, and dual-layer line patterns, can be successfully transferred. Moreover, the InTP method was used to fabricate a uniform and high-temperature film heater and an asymmetric blind film.

1. Introduction

Nanostructuring is becoming an essential process for diverse applications, such as nanoelectronics [1–3], sensors [1,4,5], metamaterials [6–8] and optics [9–12]. Nanostructures are typically fabricated using nanometer-scale lithography methods, such as electron beam lithography, deep ultraviolet lithography, and KrF laser lithography. However, these technologies remain disadvantageous because they require expensive equipment and complex fabrication processes. To overcome these problems, nanotransfer printing (nTP) has been investigated as an alternative strategy. nTP makes it possible to fabricate nanopatterns even at the sub-10-nm scale at low cost with relative simplicity [13]. Nanotransfer printing is accomplished by controlling the relative binding forces, which denotes the difference between the binding forces at the mold-pattern and pattern-substrate interfaces. Therefore, successful transfer requires either the adhesion at the mold-pattern interface to be decreased, or that at the pattern-substrate interface to be increased.

Various methods have been developed to lower the adhesion force at the mold-pattern interface: use of a thermal release film [14], reaction with liquid [15–18], surface relief structure [19–21], shear debonding [22–24], and dissolution of the stamp [25,26]. However, with these methods, it is difficult to obtain robust adhesion at the pattern-substrate interface as it relies only on weak adhesion forces, such as van der Waals forces and surface tension [25].

Therefore, adhesion at the pattern-substrate interface should be enhanced for robust transfer. For this purpose, a number of methods have been actively researched. One of the methods is the use of an additional adhesion layer (AAL) at the pattern-substrate interface. The addition of this layer enables chemical adhesion of the pattern-substrate interface, resulting in robust adhesion [27–30]. In certain cases, the same kind of metal can be utilized as AAL by using cold welding phenomena [31]. However, an AAL imposes certain limitations such as the maximum process temperature for chemical adhesion and restriction of the kind of metal for cold welding (the same kind of metal as that intended for adhesion). Both of these methods induce changes in the optical characteristics, which is important for meta-optical applications.

Efforts to exclude the use of an AAL have recently led to the development of two methods. The first method utilizes the glass transition temperature (T_g) of the substrate polymer. When the polymer is heated to its T_g, the surface of the polymer is partially deformed; consequently, a conformal contact in the pattern-substrate interface can be formed. This conformal contact can maximize the van der Waals force and thus enables the pattern to be transferred [25,32]. However, the adhesion that can be achieved by conformal contact is still limited as the van der

* Corresponding authors.
E-mail addresses: inkyu@kaist.ac.kr (I. Park), jhjeong@kimm.re.kr (J.-h. Jeong).

https://doi.org/10.1016/j.apsusc.2021.149500
Received 23 November 2020; Received in revised form 26 January 2021; Accepted 6 March 2021
Available online 14 March 2021

Waals force, which is determined by the intrinsic property of individual interfaces, is the main adhesion force. The second method utilizes the physical morphology of the transferred pattern, i.e., embedding. By embedding the patterns into the substrate, the adhesion of the pattern-substrate interface can be significantly enhanced without an AAL [33–39]. However, this method needs intentional penetration of the nanopatterns into the substrate, which requires nanostructures with high aspect ratios or bottom-enlarged shapes.

In this work, to address the aforementioned limitations and adopt the advantages of both methods, we propose a novel AAL-free, simple, versatile, and robust nanotransfer process that we named the imidization-induced nTP (InTP) method. The proposed method is based on a mechanical interlocking mechanism that occurs during the imidization process. The metal pattern is initially transferred via conformal contact at the metal-polymer interface. Next, adhesion strengthening is realized via mechanical interlocking of the penetrated metal patterns. Rather than being enabled by complex morphologies, the penetration of the pattern takes place as a result of thermal reflow of the polymer during the imidization process. This method is useful not only for strengthening the adhesion to well-transferable metal patterns (e.g., Au or Ag) but also for enabling poorly transferable materials such as Ni to be transferred.

2. Experimental section

2.1. Fabrication of PUA replicated mold

The Si master mold was fabricated using KrF optical lithography and reactive ion etching processing. The surface of the fabricated Si master mold was treated with trichloro(1H,1H,2H,2H-perfluoroctyl)silane (FOTS, Sigma-Aldrich, USA) at 80 ℃ for 25 min to improve its detachability from the polymer (FOTS treatment). The replicated mold was fabricated by applying a coating of UV-curable polyurethane acrylate (PUA) resin (311-RM, Minuta Tech. Co., Ltd, Korea) on the Si master mold. This sample was further covered with a poly(ethylene terephthalate) (PET) film with a thickness of 100 μm using a hand roller. The coated resin was cured by exposure to UV light for 90 s. After detachment, the reverse side of the PUA replicated mold was also exposed to UV light. Subsequently, e-beam deposition (Daeki Hi-Tech, Co., Ltd, Korea) was used to deposit metal (at least 99.99% pure) on the polymerized PUA replicated mold. The deposition speed was controlled at 2–3 Å/s. Details of the experimental conditions and the type and thickness of metals and metal layers can be found in Table S2.

2.2. Transfer of nanopatterns

Polyimide (PI) varnish (PI-1388, Vtec, USA) was spin-coated at a rotating speed of 2,000 rpm for 30 s and dried on a hot plate at a temperature of 150 ℃ for 3 min. On the soft baked polyamic acid (PAA) film, the transfer was conducted with custom-built roll-to-plate nanotransfer equipment (Figure S1a), in a temperature range of 140–180 ℃, at a contact force of 40–50 N, and at a rolling speed of 5 mm/s. The transfer was followed by an annealing process of which the details are summarized in Table S2 (partial imidization). After partial imidization, the PUA replicated mold was detached from the PAA substrate, and the PAA film was subjected to a full imidization process on a hot plate at 260 ℃ for 1 h.

2.3. Fabrication of 3D nanostructures

In the case of the asymmetric sidewall patterns, the metal sidewall was formed using oblique angle deposition on the replicated mold and was transferred. The oblique angle deposition was performed by tilting the deposition plane at an angle of 38° within an e-beam evaporator and depositing a layer of approximately 48.7 nm thick, with an expected deposit of 30 nm on the sidewall. This deposition was conducted without rotation of the deposition plane. After fabrication of the metal-coated replicated mold, the transfer was performed under the conditions shown in Table S2. In the case of suspended nanowire patterns, the PAA film was patterned beforehand, and the metal nanowire was transferred onto the patterned PAA substrate. First, the PI varnish was spin-coated onto the PUA mold at 1000 rpm for 30 s and dried for 3 min on a hot plate at a temperature of 150 ℃. This mold pattern was transferred onto the PAA substrate at a temperature of 170 ℃, after which the PUA mold was detached without undergoing further thermal annealing. The metal nanoline pattern was transferred onto the patterned PAA film at a temperature of 170 ℃ for 5 min. The detailed conditions of the transfer process can be found in Table S2. In the case of dual-layer nanoline patterns, two nanowire patterns were transferred onto the same PAA substrate sequentially. First, the lower line pattern was transferred, and next, the upper line pattern was transferred directly onto the lower line pattern with an orientation perpendicular to the lower line pattern. Detailed conditions of the transfer can be found in Table S2.

2.4. Fabrication of the film heater

Silver paste (P-100, CANS, Japan) was used to attached electrical wires to the side of the heater consisting of the transferred Au square mesh pattern with a pitch of 1000 nm and width of 200 nm.

2.5. Details of the sample analysis process

Details of the equipment used in this study are listed in Table S3. The sheet resistance was measured at the center region of the transferred sample and used as the representative value. In the case of the FTIR analysis, the baseline was corrected using the asymmetric least squares smoothing method provided by OriginLab. After the baseline correction, the variation between samples was normalized using the peak at 1500 cm^{-1} (benzene ring stretch), which is not affected by imidization [24]. The temperature of the fabricated heater was monitored by attaching a thermocouple to the center of the heater. Because the limit of measurement of the IR camera is 280 ℃, it was impossible to obtain the precise temperature distribution of the film heater at a driving voltage of 15 V. Thus, the reliability of the temperature of the IR image was verified by obtaining the reference temperature with the aid of a resistance temperature detector (RTD). The attached RTD lowered the temperature in the IR image. The difference between the RTD and IR images was measured to be less than 10 ℃.

3. Results and discussion

3.1. InTP: Principles and methods

Interfacial adhesion can be achieved in various ways: the use of surface and field forces, such as van der Waals forces; material bridges, such as mechanical interlocking; shape effects, such as capillary forces; and suction forces [40]. Among them, we adopted van der Waals forces and mechanical interlocking to ensure that InTP is highly robust.

The imidization of polyimide (PI) entails the use of three steps to form the film: coating with varnish, drying the solvent, and imidization. Once the solvent has dried, the film exists in the form of polyamic acid (PAA), which has thermoplastic properties. After the imidization process, the film exists in the form of PI, which has thermoset properties. The imidization process induces the thermal reflow of the polymer film by high-temperature heating [41,42]. Herein, these features are adopted to transfer and reinforce the adhesion, as detailed in the following.

First, the pattern is transferred via conformal contact between the pattern and substrate (Fig. 1a-i). Owing to the thermoplastic properties of the PAA substrate, it is possible to reshape the substrate surface when the temperature exceeds the T_g of PAA. This process enables the PAA substrate to engage in conformal contact with the pattern and thus enables pattern transfer. Transfer experiments were carried out at various

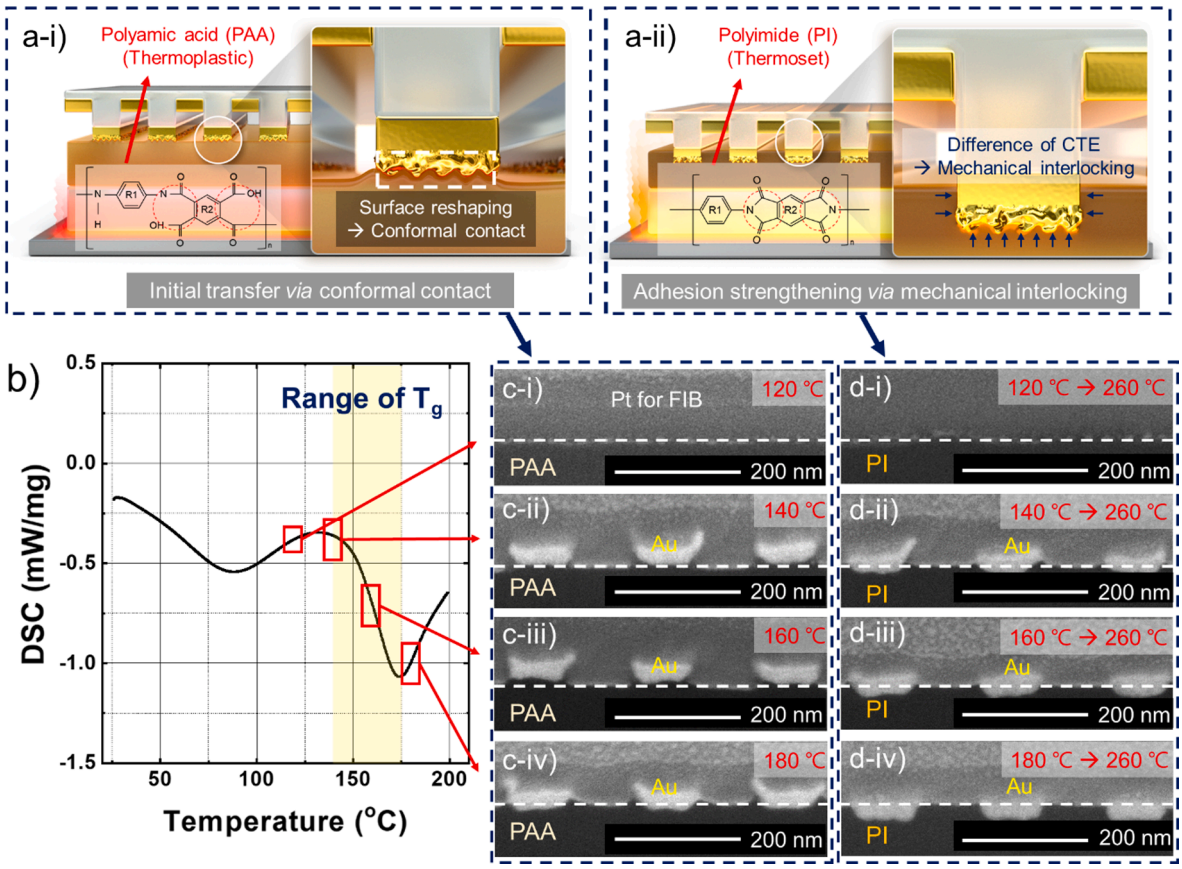

Fig. 1. Principles of imidization-induced nanotransfer (InTP): a) Schematic of InTP. Initially, the pattern is (i) transferred via conformal contact, and (ii) reinforced via mechanical interlocking; b) Differential scanning calorimetry analysis of the fabricated PAA substrate for the confirmation of the glass transition temperature (T_g); Cross-sectional images of the transfer results at various temperatures c) before and d) after imidization. The white dotted lines in panels (c) and (d) denote the boundary of the substrate.

temperatures to confirm this result. The T_g range of PAA was measured as 140–175 ℃ (Fig. 1b), and the pattern could not be transferred at temperatures below T_g (Fig. 1c-i). By contrast, the transfer results were similar as long as the temperature was above T_g. (Fig. 1c-iv). Once the process temperature exceeded 200 ℃, the mold film started to wrinkle and induced tearing and wrinkling of the substrate (Figure S1c).

Next, heating above the imidization temperature causes the polymer to reflow during imidization, and this causes the pattern to penetrate the polymer. The penetration of the pattern was confirmed by analyzing the cross-sectional images after imidization. In Fig. 1c, d, the white dotted lines denote the substrate boundary. Compared with the position of the pattern, the penetration can be observed to have occurred at all three temperatures (Fig. 1d-ii, iii, iv). After imidization, both the transferred metal nanopatterns and substrate undergo thermal shrinkage upon cooling to 25 ℃. However, the shrinking ratio is larger in PI than in the metal because of the larger thermal expansion coefficient of PI (30–65 ppm [43]) than that of metal (less than20 ppm). Thus, the greater degree of shrinkage in PI generates a mechanically interlocked state of the pattern.

X-ray photoelectron spectroscopy (XPS) was used to investigate the reason for the reinforced adhesion (Figure S2). The 4f peak of Au, which is expected to change if direct chemical bonding occurs between Au and the substrate, was monitored [28]. However, the XPS data did not reveal any changes in this peak, and thus chemical bonding may not be the dominant reason for the adhesion between PAA and the metal pattern. This led us to conclude that reinforced adhesion may be attributed to mechanical interlocking.

Based on these principles, the following steps were used in the InTP process. First, the replicated nanopattern mold is fabricated by imprinting on a silicon master mold, followed by electron beam deposition (Figure S3a). Next, the mold is transferred onto the spin-coated and solvent dried PAA substrate, as the metal nanopattern side is matched with the PAA substrate (Figure S3b). The transfer process is conducted with custom-built roll transfer equipment (Figure S1a). Additional adhesion can be provided at the pattern-substrate interface before detachment of the replicated mold by using a partial imidization process (Figure S3c). After the replicated mold is detached from the substrate, full thermal imidization is performed (Figure S3d). Details of the fabrication process are provided in the Section 2.

3.2. Characterization of InTP

Next, the effect of imidization in the adhesion was compared by conducting a scratch test. Scratch testing was chosen as the test method because the tangential force that needs to delaminate the film (nanopattern, in this research) can be measured directly.

Before imidization, the line pattern started to delaminate (Fig. 2a) with a tangential force (F_t) of 24.29 mN (Figure S4). In contrast, after imidization, it was impossible to measure the F_t at the delamination point precisely because the line pattern did not delaminate from the PI substrate (Fig. 2d-iii) before the detachment of the PI substrate from the silicon wafer (F_t = 500 mN, Figure S4). Thus, it was confirmed that the imidization process dramatically reinforces the adhesion of the pattern-substrate interface. The mechanical robustness of the transferred nanopatterns after the imidization process was also confirmed through a bending test with a curvature radius of 0.35 cm for 10,000 cycles (Figure S5). After the bending test, the change in resistance was measured to be 0.7%. The results of the scratch and bending tests

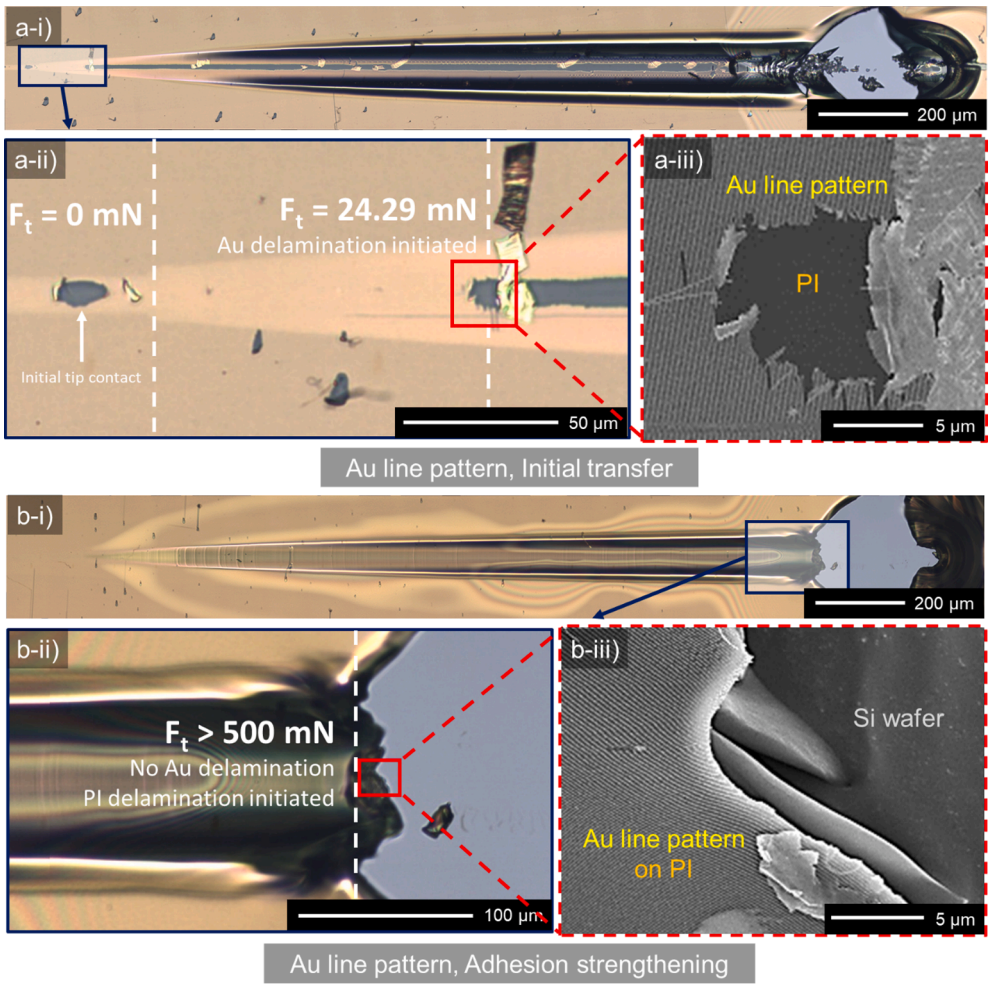

Fig. 2. Verification of the effect of imidization – Scratch test result (a) before and (b) after imidization. Imidization significantly improves the adhesion of the nanopattern (24.29 mN → >500 mN).

allowed us to conclude that imidization dramatically increased the adhesion, and that the strengthened adhesion remained stable.

In addition, apart from a line pattern, other patterns, such as hexagonal and square mesh patterns, were transferred via InTP. Because the reliability is difficult to confirm by visual inspection only, it was verified by assessing the sheet resistance of the metal pattern. A linear relationship exists between the sheet resistance and the value of k, which is defined as follows (Details of the calculation process can be found in "Calculation of Sheet Resistance of Periodic Metal Patterns" in the Supplementary Material):

Eq. (1). For the square mesh pattern:

$$\rho_s \propto \frac{r^2 - r + 1}{r} \equiv k \tag{1}$$

Eq. (2). For the hexagonal mesh pattern:

$$\rho_s \propto \frac{4r'}{\sqrt{r'^2 - 1}} \tan^{-1}\sqrt{\frac{r' + 1}{r' - 1}} - \pi + \frac{1}{\sqrt{3}} - \frac{2}{r'} \equiv k \tag{2}$$

where ρ_s is the sheet resistance, $r = a/d$, and $r' = a\sqrt{3}/d$, where a is the pitch, and d is the mesh width (diameter of the dot). The experimental results for different mesh patterns satisfied the suggested linear relationship (Figure S6). This implies that the patterns are well transferred without significant defects.

3.3. InTP for versatile materials

Because of the low intrinsic ability of Au to adhere to the mold, successful transfer can be achieved by using a simple transfer process that adopts conformal contact. However, in the case of Ni, transfer is difficult owing to its strong adhesion to the mold. For comparison, dot array patterns of Au (Fig. 3a-i) and Ni (Fig. 3a-ii) were transferred under the same conditions, i.e., annealing at 170 ℃ for 1 min after roll transfer. To minimize the unintentional connection among metal patterns, a dot-shaped pattern was adopted for this experiment. The Au pattern was successfully transferred, but the Ni pattern was only partially transferred (Fig. 3a-ii, region enclosed by the red rectangle). The successful transfer of metals with strong adhesion to molds requires additional adhesion forces before the mold can be detached. As most of the polymers, including the replicated mold used in this study, melt at the imidization temperature of PI (260 ℃), adhesion reinforcement by using the normal imidization process is difficult to apply. Instead, partial imidization at a lower temperature (170 ℃) was adopted to transfer the Ni pattern [44].

First, partial imidization of the PAA substrate at 170 ℃ was confirmed with Fourier transform infrared (FTIR) spectroscopy (Fig. 3b). Five samples were prepared and analyzed: original PAA, PAA annealed for 1 min, 3 min, and 5 min, and fully imidized PI. The bands at 1775 cm^{-1} (C = O asymmetric stretching), 1375 cm^{-1} (C-N stretching), and 723 cm^{-1} (imide-five-ring deformation vibration) were shown to depend on the degree of imidization (ID) [45–47]. The FTIR results confirmed that these three peaks changed in accordance with the ID. For comparison, experiments were conducted by varying the annealing

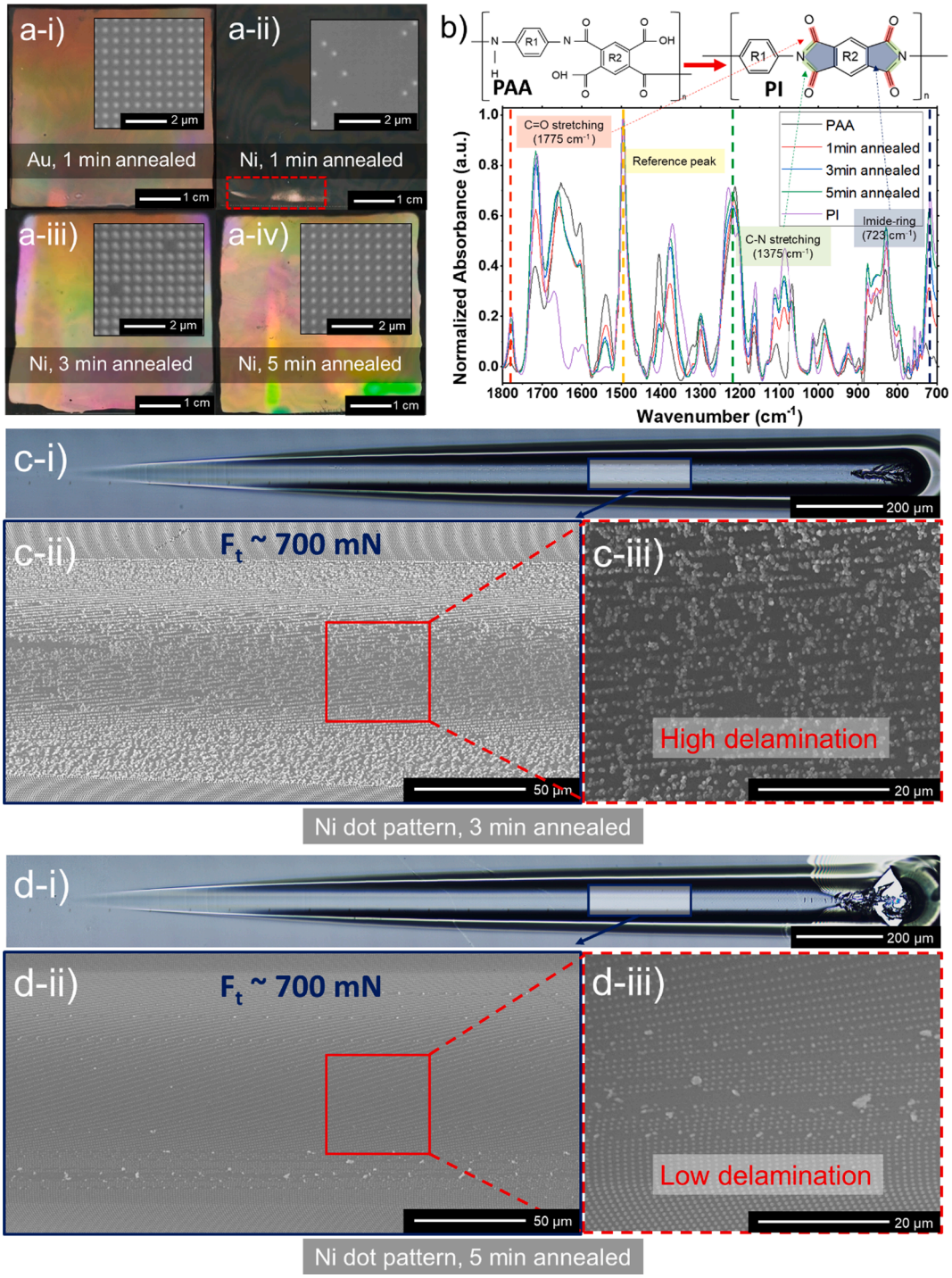

Fig. 3. a) Dependence of the transfer results on the metal and annealing time. Inset: Enlargement of the fabricated patterns (optical microscopy). An increase in the annealing time enables the metal nanopatterns to be transferred reliably; b) Comparison of the dependence of the imidization degree on the annealing time (FTIR spectroscopy). An increase in the annealing time increases the degree of imidization of the substrate; Scratch test result of c) 3 min and d) 5 min annealed Ni dot pattern without imidization. An increase in the annealing time increases the robustness of the pattern-substrate adhesion.

time: 1 min (Fig. 3a-ii), 3 min (Fig. 3a-iii), and 5 min (Fig. 3a-iv). The sample with an annealing time of 1 min was not transferred satisfactorily, whereas the samples with annealing times of 3 min and 5 min were successfully transferred. In the case of the samples with a 3 min annealing time, certain dots failed to be transferred because of the insufficient adhesion force (Fig. 3a-iii, inset). In contrast, all the patterns of the samples processed with a 5 min annealing time were completely transferred owing to reinforced adhesion (Fig. 3a-iv, inset). The scratch test revealed the same tendency; a few spots of the dot patterns in the sample with the 3 min annealing time were extensively delaminated (Fig. 3c), whereas the sample with the 5 min annealing time underwent less delamination (Fig. 3d) for the same tangential force (Figure S7). Therefore, it can be concluded that the Ni pattern was more strongly adhered to the PAA substrate as a result of the longer annealing period. These experiments confirmed that pattern adhesion can be reinforced by partial imidization of the PAA substrate for appropriate time periods. In an attempt to confirm these results, a variety of metals (200 nm pitch, 100 nm wide line pattern) were transferred using the same method.

Diverse metals, such as Ni (Fig. 4a-i), Pd (Fig. 4a-ii), Ag (Fig. 4a-iii), and Cu (Fig. 4a-iv) were successfully transferred.

3.4. Fabrication of various 3D structures

Because the proposed InTP method allows robust adhesion, it is suitable for transferring patterns with a smaller contact area between the pattern and substrate than that between the pattern and the mold. The ratio (r) of the contact area between the pattern and mold to that between the pattern and substrate was defined for the analysis. First, an asymmetric sidewall pattern with r = 3.5 was fabricated (Fig. 5a) through slanted angle deposition on the mold with nanoline patterns. Despite the large r-value, it was possible to transfer the asymmetric sidewall pattern successfully owing to the strong adhesion resulting from the InTP process. Second, a suspended nanowire array pattern with r = 1.7 was fabricated (Fig. 5b). The PAA substrate was first patterned as a line pattern, after which the metal nanowire array was successfully transferred onto it. These kinds of structures can be used in chemical or biological sensing applications that require a high surface-to-volume ratio [48–51]. Lastly, a dual-layer line pattern was fabricated (Fig. 5c) by transferring two line patterns perpendicular to each other in sequence. Even though the r-value for the second line layer exceeded 2, the layer was successfully transferred on top of the first layer. Additional transmission electron microscopy (TEM) analysis was performed to observe the morphology (Fig. 5c-iii). The TEM image revealed that the nanogap between the upper and lower layers was less than 20 nm wide. This nanogap is expected to be useful for surface enhanced Raman spectroscopy applications [18,52–54].

3.5. Application to high-temperature heater film and asymmetric blind film

3.5.1. High-temperature heater film

Film heaters are widely used components in various applications, such as in wearable electronics and for window defogging [55–57]. These heaters are typically fabricated by applying a layer of silver nanowires (AgNWs) using spray coating because of the simple fabrication process and low sheet resistance of AgNWs. However, this method may be disadvantageous for use at temperatures in excess of 200 ℃ (melting temperature of the AgNWs [58–60]). Thus, alternative conductive nanomaterials, such as carbon nanotubes or graphene, have been introduced to achieve high-temperature heating. However, the high sheet resistance of these materials requires the application of high driving voltages to realize high-temperature heating. These problems (i.e., low maximum heating temperature and high driving voltage) can be resolved by transferring the nanopatterns of metals of which the melting temperatures are higher than that of Ag. Furthermore, uniformly aligned nanopatterns would be able to improve the temperature uniformity.

In this work, we fabricated a heater composed of the Au mesh pattern with a thickness of 30 nm, as shown in Figure S5a. The heating test of the fabricated heater was performed with the experimental setup shown in Fig. 6a. The heating test was carried out with applied voltages of 3, 6, 9, 12, and 15 V (Fig. 6b). Each cycle consisted of three minutes of heating (voltage applied) and three minutes of cooling (voltage relieved). Using

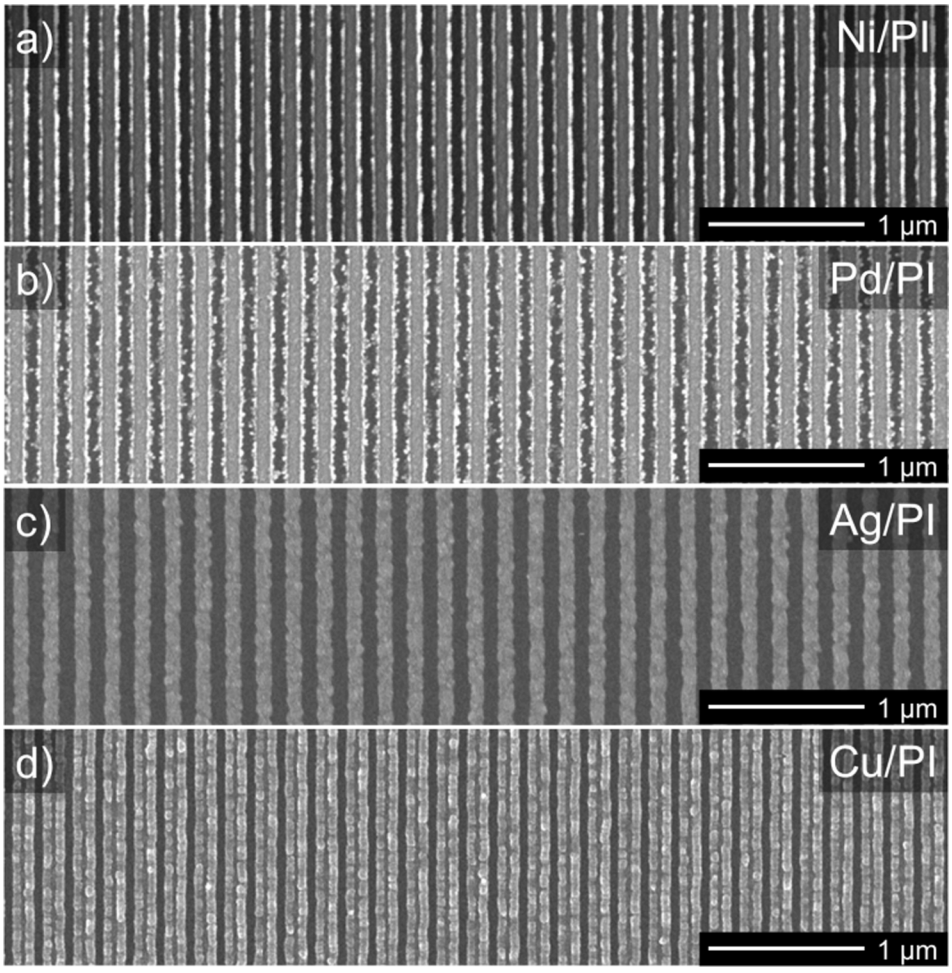

Fig. 4. Result of transferring the metal nanopattern from the mold, in this case a line pattern with a width of 100 nm and pitch of 200 nm, which is composed of a) nickel, b) palladium, c) silver, and d) copper.

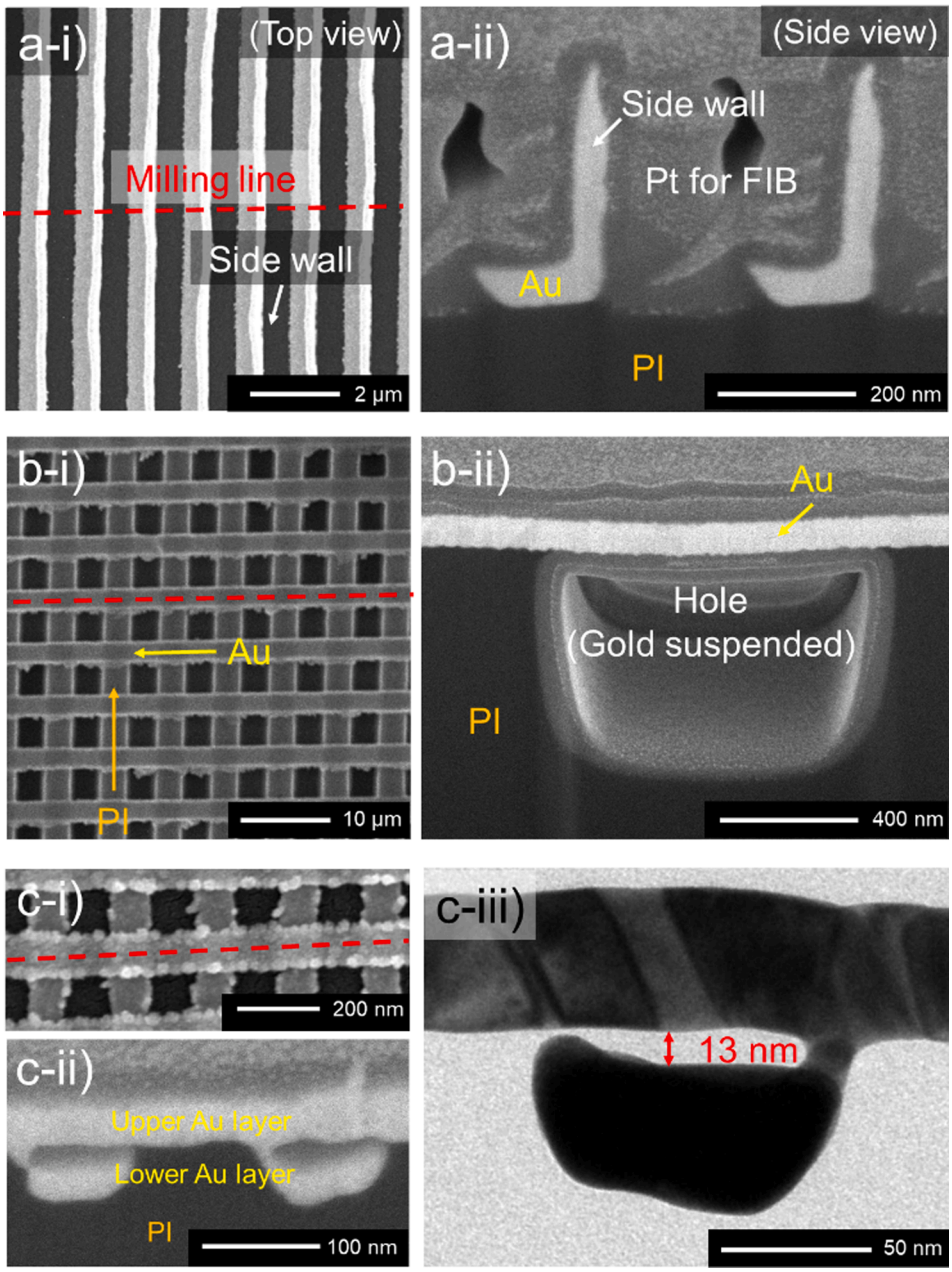

Fig. 5. Result of 3D structuring: a) Fabricated asymmetric sidewall pattern; b) Fabricated suspended nanowire pattern; c) Fabricated dual-layer line pattern with the iii) TEM image. For the side view image, the milling line, indicated in the top view, was cut using FIB, and the pattern was observed using SEM.

a low driving voltage of 15 V, the heater film was capable of high-temperature heating to temperatures exceeding 300 ℃ without failure or degradation during repeated heating–cooling cycles. Moreover, infrared (IR) imaging (Fig. 6c) proved the temperature uniformity during heating periods with driving voltages of 3, 9, and 15 V. Our heater film achieved a higher temperature (300 ℃) than previously developed film heaters (Table S1). Furthermore, it has a highly reliable (Fig. 6b) and uniform (Fig. 6c) heating capability. These advantages could possibly be attributed to the fact that Au has a higher melting temperature than Ag. In addition, the high robustness of the InTP process enables the uniform metal nanopatterns on the replicated mold to be successfully transferred onto the polymer substrates without significant defects. This ensures that the heater has uniform heating behavior and that unintended energy focusing regions, which are mainly caused by defects, are mostly eliminated.

3.5.2. Asymmetric blind film

The InTP method can be used to easily transfer not only planar nanopatterns but also 3D nanostructures onto the substrate. We fabricated asymmetric wall-shaped 3D nanostructures (Fig. 5a) and used them as an asymmetric blind film. Because of the asymmetry, the optical transmittance of the film depends on the incident angle of the light. Based on the focused ion beam (FIB) image, the maximum transmittance was calculated to occur in the incident angle range 0–30°. In addition, the film was not transparent to light below an incident angle of −38° (Fig. 6d). This tendency was confirmed with UV–visible spectroscopy (UV–Vis). Compared with the higher transmittance at incident angles of 0° and 30°, the transmittance at an incident angle of −40° was dramatically reduced (Fig. 6e). At the wavelength of 620 nm, the transmittance decreased by approximately 5 times compared with its initial value by changing the incident angle from 30° to −40°. For comparison purposes, demo images were obtained at various incident

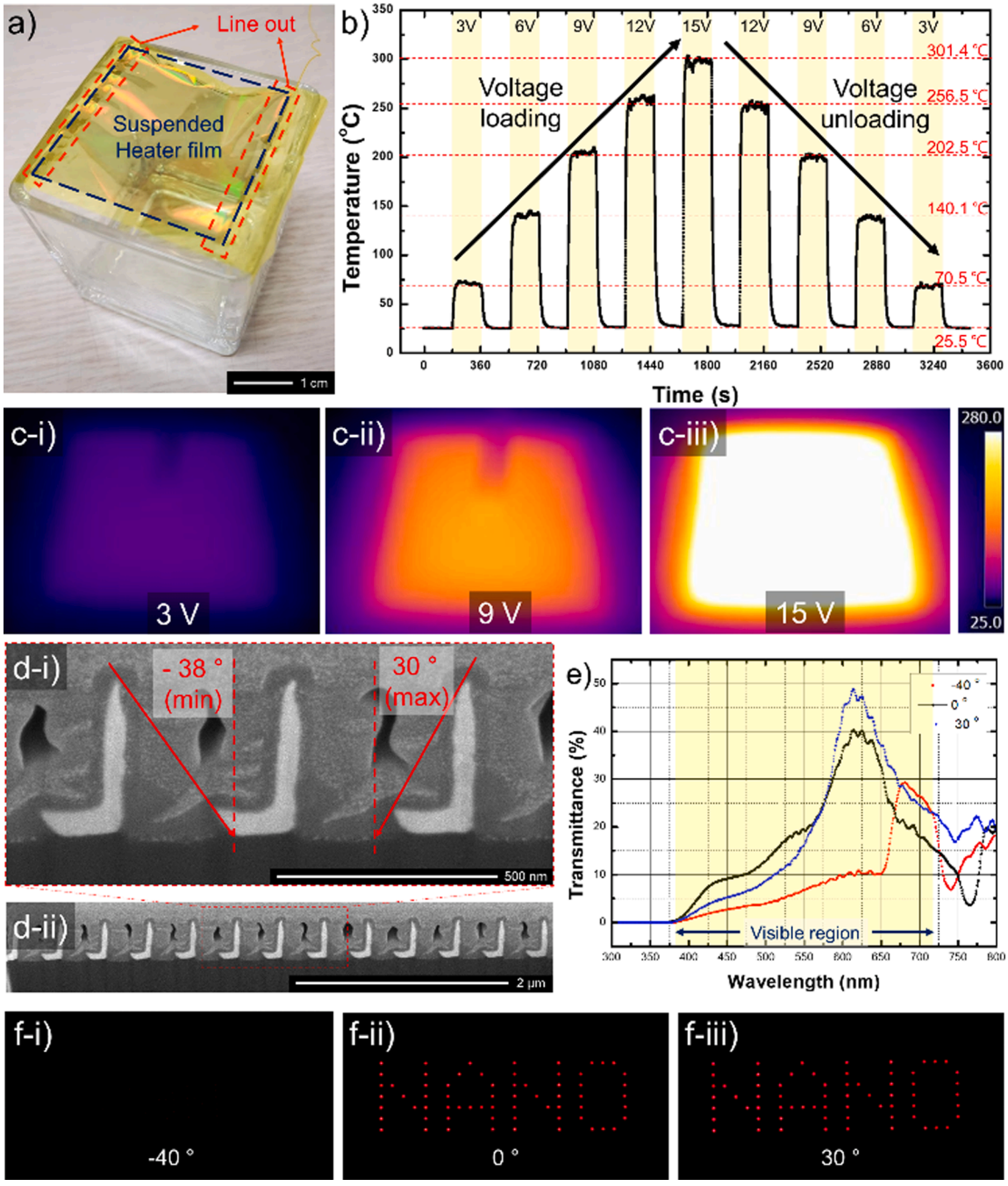

Fig. 6. Experimental results for the applications: a) Image of the fabricated heater with heating area of 4 cm × 4 cm; b) Result of the voltage loading / unloading experiment. At 15 V, the temperature of the heater achieved over 300 ℃; c) IR image of the heater with an applied voltage of i) 3 V, ii) 9 V, and iii) 15 V; d) Cross-sectional view of the asymmetric wall pattern (i) and its wide view (ii). The result showed that the transmittance is maximized and minimized at incident angles of 30° and −38°, respectively; e) Dependence of the measured transmittance on the incident angle; f) Demo image of the selective blind at incident angles of i) −40°, ii) 0°, and iii) 30°.

angles (Fig. 6f). The experimental setup used to capture these images is shown in Figure S8. At an incident angle of −40°, the word "NANO" is not displayed owing to the blockage of light. By contrast, this word is clearly visible at incident angles of 0° and 30° owing to the much higher optical transmittance. This different optical transmittance can be attributed to the high aspect ratio of the 3D asymmetric nanostructures that were fabricated using the InTP process.

4. Conclusions

In this research, nanopatterns with various morphologies (linear, hexagonal mesh, square mesh, and dots) and consisting of various materials (Au, Pd, Ag, Cu, and Ni) were successfully transferred onto a PI substrate using the proposed InTP method. The superior adhesion provided by mechanical interlocking by using the InTP process allowed for the robust transfer of various nanopatterns and 3D nanostructures, such as an asymmetric sidewall, suspended nanowire, and dual-layer line patterns. The versatility and uniformity of InTP enabled a film heater with high-temperature stability and low bias voltage (>300 ℃, 15 V) operation to be fabricated. In addition, the robust and 3D nanostructurable features of the InTP allowed for the fabrication of an asymmetric blind film. The nanotransfer process using the proposed

InTP method offers substantial advantages, such as versatility, uniformity, and reliability. Considering that few nanotransfer-based printing methods capable of reinforced adhesion without using any AAL have been reported to date, we foresee this method to be widely used for the fabrication of various nanopatterns in nanoelectronics, nanosensors, and flexible electronics applications in future.

Funding

This work was supported by the Center for Advanced Meta-Materials (CAMM) funded by the Ministry of Science, ICT, and Future Planning as Global Frontier Project (CAMM No. 2014M3A6B3063707). This project was supported by Institute of Information & Communications Technology Planning & Evaluation (IITP) grant funded by the Korea government (MSIT) (No. 2020-0-00914, Development of hologram printing downsizing technology based on holographic optical element (HOE)). This project was supported by the Basic Research Program of KIMM (Korea Institute of Machinery and Materials, NK230C). This work was supported by a National Research Foundation of Korea (NRF) grant funded by the Korean government (MSIT) (No. 2021R1A2C3008742).

Declaration of Competing Interest

The author declare that there is no conflict of interest.

Appendix A. Supplementary material

Supplementary data to this article can be found online at https://doi.org/10.1016/j.apsusc.2021.149500.

References

[1] J.Y. Yoo, M.H. Seo, J.S. Lee, K.W. Choi, M.S. Jo, J.B. Yoon, Industrial grade, bending-insensitive, transparent nanoforce touch sensor via enhanced percolation effect in a hierarchical nanocomposite film, Adv. Funct. Mater. 28 (2018) 1–8, https://doi.org/10.1002/adfm.201804721.

[2] M.H. Seo, S.J. Choi, S.H. Park, J.Y. Yoo, S.K. Lim, J.S. Lee, K.W. Choi, M.S. Jo, I. D. Kim, J.B. Yoon, Material-independent nanotransfer onto a flexible substrate using mechanical-interlocking structure, ACS Nano 12 (2018) 4387–4397, https://doi.org/10.1021/acsnano.8b00159.

[3] K. Tanabe, K. Watanabe, Y. Arakawa, Flexible thin-film InAs/GaAs quantum dot solar cells, Appl. Phys. Lett. 100 (2012), 192102, https://doi.org/10.1063/1.4712597.

[4] J.-S. Lee, M.-H. Seo, K.-W. Choi, J.-Y. Yoo, M.-S. Jo, J.-B. Yoon, Stress-engineered palladium nanowires for wide range (0.1%–3.9%) of H 2 detection with high durability, Nanoscale. 11 (2019) 16317–16326, https://doi.org/10.1039/c9nr01975h.

[5] M. Melzer, D. Karnaushenko, G. Lin, S. Baunack, D. Makarov, O.G. Schmidt, Direct transfer of magnetic sensor devices to elastomeric supports for stretchable electronics, Adv. Mater. 27 (2015) 1333–1338, https://doi.org/10.1002/adma.201403998.

[6] L. Gao, K. Shigeta, A. Vazquez-Guardado, C.J. Progler, G.R. Bogart, J.A. Rogers, D. Chanda, Nanoimprinting techniques for large-area three-dimensional negative index metamaterials with operation in the visible and telecom bands, ACS Nano 8 (2014) 5535–5542, https://doi.org/10.1021/nn5015775.

[7] L. Gao, Y. Kim, A. Vazquez-Guardado, K. Shigeta, S. Hartanto, D. Franklin, C. J. Progler, G.R. Bogart, J.A. Rogers, D. Chanda, Materials selections and growth conditions for large-area, multilayered, visible negative index metamaterials formed by nanotransfer printing, Adv. Opt. Mater. 2 (2014) 256–261, https://doi.org/10.1002/adom.201300356.

[8] D. Chanda, K. Shigeta, S. Gupta, T. Cain, A. Carlson, A. Mihi, A.J. Baca, G. R. Bogart, P. Braun, J.A. Rogers, Large-area flexible 3D optical negative index metamaterial formed by nanotransfer printing, Nat. Nanotechnol. 6 (2011) 402–407, https://doi.org/10.1038/nnano.2011.82.

[9] Z.J. Zhao, M. Lee, H. Kang, S. Hwang, S. Jeon, N. Park, S.H. Park, J.H. Jeong, Eight inch wafer-scale flexible polarization-dependent color filters with Ag-TiO 2 composite nanowires, ACS Appl. Mater. Interfaces. 10 (2018) 9188–9196, https://doi.org/10.1021/acsami.8b02128.

[10] Z.J. Zhao, M. Gao, S.H. Hwang, S. Jeon, I. Park, S.H. Park, J.H. Jeong, Heterogeneous Nanostructures fabricated via binding energy-controlled nanowelding, ACS Appl. Mater. Interfaces. 11 (2019) 7261–7271, https://doi.org/10.1021/acsami.8b18405.

[11] Z.J. Zhao, S.H. Hwang, S. Jeon, B. Hwang, J.Y. Jung, J. Lee, S.H. Park, J.H. Jeong, Three-dimensional plasmonic Ag/TiO_2 nanocomposite architectures on flexible substrates for visible-light photocatalytic activity, Sci. Rep. 7 (2017) 1–11, https://doi.org/10.1038/s41598-017-09401-z.

[12] S.H. Hwang, J. Cho, S. Jeon, H.J. Kang, Z.J. Zhao, S. Park, Y. Lee, J. Lee, M. Kim, J. Hahn, B. Lee, J.H. Jeong, H. Kim, J.R. Youn, Gold-nanocluster-assisted nanotransfer printing method for metasurface hologram fabrication, Sci. Rep. 9 (2019) 1–12, https://doi.org/10.1038/s41598-019-38891-2.

[13] J.H. Lee, H.J. Choi, C. Lee, S.W. Song, J.B. Lee, D. Huh, Y.S. Nam, D.Y. Jeon, H. Lee, Y.S. Jung, Spontaneous registration of Sub-10 nm features based on subzero celsius spin-casting of self-assembling building blocks directed by chemically encoded surfaces, ACS Nano 12 (2018) 8224–8233, https://doi.org/10.1021/acsnano.8b03378.

[14] Z. Yan, T. Pan, M. Xue, C. Chen, Y. Cui, G. Yao, L. Huang, F. Liao, W. Jing, H. Zhang, M. Gao, D. Guo, Y. Xia, Y. Lin, Thermal release transfer printing for stretchable conformal bioelectronics, Adv. Sci. 4 (2017) 1700251, https://doi.org/10.1002/advs.201700251.

[15] C.H. Lee, D.R. Kim, X. Zheng, Fabrication of nanowire electronics on nonconventional substrates by water-assisted transfer printing method, Nano Lett. 11 (2011) 3435–3439, https://doi.org/10.1021/nl201901z.

[16] C.H. Lee, D.R. Kim, X. Zheng, Transfer printing methods for flexible thin film solar cells: Basic concepts and working principles, ACS Nano 8 (2014) 8746–8756, https://doi.org/10.1021/nn5037587.

[17] J. Zhao, Y. Guo, L. Cai, H. Li, K.X. Wang, I.S. Cho, C.H. Lee, S. Fan, X. Zheng, High-performance ultrathin BiVO4 photoanode on textured polydimethylsiloxane substrates for solar water splitting, ACS Energy Lett. 1 (2016) 68–75, https://doi.org/10.1021/acsenergylett.6b00032.

[18] J.W. Jeong, S.R. Yang, Y.H. Hur, S.W. Kim, K.M. Baek, S. Yim, H.I. Jang, J.H. Park, S.Y. Lee, C.O. Park, Y.S. Jung, High-resolution nanotransfer printing applicable to diverse surfaces via interface-targeted adhesion switching, Nat. Commun. 5 (2014) 1–12, https://doi.org/10.1038/ncomms6387.

[19] H. Chen, X. Feng, Y. Huang, Y. Huang, J.A. Rogers, Experiments and viscoelastic analysis of peel test with patterned strips for applications to transfer printing, J. Mech. Phys. Solids. 61 (2013) 1737–1752, https://doi.org/10.1016/j.jmps.2013.04.001.

[20] H. Chen, X. Feng, Y. Chen, Directionally controlled transfer printing using micropatterned stamps, Appl. Phys. Lett. 103 (2013), 151607, https://doi.org/10.1063/1.4824976.

[21] J. Jeong, J. Kim, K. Song, K. Autumn, J. Lee, Geckoprinting: assembly of microelectronic devices on unconventional surfaces by transfer printing with isolated gecko setal arrays, J. R. Soc. Interface. 11 (2014) 20140627, https://doi.org/10.1098/rsif.2014.0627.

[22] A. Carlson, H.J. Kim-Lee, J. Wu, P. Elvikis, H. Cheng, A. Kovalsky, S. Elgan, Q. Yu, P.M. Ferreira, Y. Huang, K.T. Turner, J.A. Rogers, Shear-enhanced adhesiveless transfer printing for use in deterministic materials assembly, Appl. Phys. Lett. 98 (2011) 2009–2012, https://doi.org/10.1063/1.3605558.

[23] S.Y. Yang, A. Carlson, H. Cheng, Q. Yu, N. Ahmed, J. Wu, S. Kim, M. Sitti, P. M. Ferreira, Y. Huang, J.A. Rogers, Elastomer surfaces with directionally dependent adhesion strength and their use in transfer printing with continuous roll-to-roll applications, Adv. Mater. 24 (2012) 2117–2122, https://doi.org/10.1002/adma.201104975.

[24] H. Cheng, J. Wu, Q. Yu, H.J. Kim-Lee, A. Carlson, K.T. Turner, K.C. Hwang, Y. Huang, J.A. Rogers, An analytical model for shear-enhanced adhesiveless transfer printing, Mech. Res. Commun. 43 (2012) 46–49, https://doi.org/10.1016/j.mechrescom.2012.02.011.

[25] R.F. Tiefenauer, K. Tybrandt, M. Aramesh, J. Vörös, Fast and versatile multiscale patterning by combining template-stripping with nanotransfer printing, ACS Nano 12 (2018) 2514–2520, https://doi.org/10.1021/acsnano.7b08290.

[26] C. Zheng, Y. Shen, M. Liu, W. Liu, S. Wu, C. Jin, Layer-by-layer assembly of three-dimensional optical functional nanostructures, ACS Nano 13 (2019) 5583–5590, https://doi.org/10.1021/acsnano.9b00549.

[27] J.B.K. Law, R.T.T. Khoo, B.S. Tan, H.Y. Low, Selective gold nano-patterning on flexible polymer substrate via concurrent nanoimprinting and nanotransfer printing, Appl. Surf. Sci. 258 (2011) 748–754, https://doi.org/10.1016/j.apsusc.2011.08.065.

[28] S.H. Hwang, Z.J. Zhao, S. Jeon, H. Kang, J. Ahn, J.H. Jeong, Repeatable and metal-independent nanotransfer printing based on metal oxidation for plasmonic color filters, Nanoscale. 11 (2019) 11128–11137, https://doi.org/10.1039/c9nr00176j.

[29] S.H. Hwang, S. Jeon, M.J. Kim, D.G. Choi, J.H. Choi, J.Y. Jung, K.S. Kim, J. Lee, J. H. Jeong, J.R. Youn, Covalent bonding-assisted nanotransfer lithography for the fabrication of plasmonic nano-optical elements, Nanoscale. 9 (2017) 14335–14346, https://doi.org/10.1039/c7nr02666h.

[30] Y.L. Loo, R.L. Willett, K.W. Baldwin, J.A. Rogers, Interfacial chemistries for nanoscale transfer printing, J. Am. Chem. Soc. 124 (2002) 7654–7655, https://doi.org/10.1021/ja026355v.

[31] C. Kim, P.E. Burrows, S.R. Forrest, Micropatterning of organic electronic devices by cold-welding, Science (80-.). 288 (2000) 831–833. doi: 10.1126/science.288.5467.831.

[32] Z.J. Zhao, S.H. Hwang, H.J. Kang, S. Jeon, M. Bok, S. Ahn, D. Im, J. Hahn, H. Kim, J.H. Jeong, Adhesive-layer-free and double-faced nanotransfer lithography for a flexible large-area metasurface hologram, ACS Appl. Mater. Interfaces. 12 (2020) 1737–1745, https://doi.org/10.1021/acsami.9b14345.

[33] X. Chen, W. Guo, L. Xie, C. Wei, J. Zhuang, W. Su, Z. Cui, Embedded Ag/Ni metal-mesh with low surface roughness as transparent conductive electrode for optoelectronic applications, ACS Appl. Mater. Interfaces. 9 (2017) 37048–37054, https://doi.org/10.1021/acsami.7b11779.

[34] A. Khan, S. Lee, T. Jang, Z. Xiong, C. Zhang, J. Tang, L.J. Guo, L. Wen-Di, High-performance flexible transparent electrode with an embedded metal mesh fabricated by cost-effective solution process, Small. 12 (2016) 3021–3030, https://doi.org/10.1002/smll.201600309.

[35] Y.H. Liu, J.L. Xu, S. Shen, X.L. Cai, L. Sen Chen, S.D. Wang, High-performance, ultra-flexible and transparent embedded metallic mesh electrodes by selective electrodeposition for all-solid-state supercapacitor applications, J. Mater. Chem. A. 5 (2017) 9032–9041, https://doi.org/10.1039/c7ta01947e.
[36] H.J. Choi, S. Choo, P.H. Jung, J.H. Shin, Y.D. Kim, H. Lee, Uniformly embedded silver nanomesh as highly bendable transparent conducting electrode, Nanotechnology. 26 (2015), https://doi.org/10.1088/0957-4484/26/5/055305.
[37] S. Yu, H.J. Han, J.M. Kim, S. Yim, D.M. Sim, H. Lim, J.H. Lee, W.I. Park, J.H. Park, K.H. Kim, Y.S. Jung, Area-selective lift-off mechanism based on dual-triggered interfacial adhesion switching: highly facile fabrication of flexible nanomesh electrode, ACS Nano 11 (2017) 3506–3516, https://doi.org/10.1021/acsnano.7b00229.
[38] C. Stuart, H.K. Park, Y. Chen, Fabrication of a 3D nanoscale crossbar circuit by nanotransfer-printing lithography, Small. 6 (2010) 1663–1668, https://doi.org/10.1002/smll.201000514.
[39] K.J. Lee, M.J. Motala, M.A. Meitl, W.R. Childs, E. Menard, A.K. Shim, J.A. Rogers, R.G. Nuzzo, Large-area, selective transfer of microstructured silicon: a printing-based approach to high-performance thin-film transistors supported on flexible substrates, Adv. Mater. 17 (2005) 2332–2336, https://doi.org/10.1002/adma.200500578.
[40] Z. Gu, S. Li, F. Zhang, S. Wang, Understanding surface adhesion in nature: a peeling model, Adv. Sci. 3 (2016) 1–13, https://doi.org/10.1002/advs.201500327.
[41] C.I. Cano, M.L. Clark, T. Kyu, R.B. Pipes, Modeling particle inflation from poly (amic acid) powdered precursors. III. Experimental determination of kinetic parameters, Polym. Eng. Sci. 48 (2008) 617–626, https://doi.org/10.1002/pen.20962.
[42] W. Chen, W. Chen, B. Zhang, S. Yang, C.Y. Liu, Thermal imidization process of polyimide film: interplay between solvent evaporation and imidization, Polymer (Guildf). 109 (2017) 205–215, https://doi.org/10.1016/j.polymer.2016.12.037.
[43] S. Numata, S. Oohara, K. Fujisaki, J. Imaizumi, N. Kinjo, Thermal expansion behavior of various aromatic polyimides, J. Appl. Polym. Sci. 31 (1986) 101–110, https://doi.org/10.1002/app.1986.070310110.
[44] S.I. Kim, S.M. Pyo, M. Ree, Investigation of glass transition behaviors in poly(amic acid) precursors of semiflexible polyimides by oscillating differential scanning calorimetry, Macromolecules 30 (1997) 7890–7897, https://doi.org/10.1021/ma970556f.
[45] J.Y. Choi, K.N. Nam, S.W. Jin, D.M. Kim, I.H. Song, H.J. Park, S. Park, C.M. Chung, Preparation and properties of poly(imide-siloxane) copolymer composite films with micro-Al_2O_3 particles, Appl. Sci. 9 (2019) 18–21, https://doi.org/10.3390/app9030548.
[46] S. Kim, K.S. Jang, H.D. Choi, S.H. Choi, S.J. Kwon, I.D. Kim, J.A. Lim, J.M. Hong, Porous polyimide membranes prepared by wet phase inversion for use in low dielectric applications, Int. J. Mol. Sci. 14 (2013) 8698–8707, https://doi.org/10.3390/ijms14058698.
[47] M. Mrsevic, D. Düsselberg, C. Staudt, Synthesis and characterization of a novel carboxyl group containing (co)polyimide with sulfur in the polymer backbone, Beilstein J. Org. Chem. 8 (2012) 776–786, https://doi.org/10.3762/bjoc.8.88.
[48] K. Kang, D. Yang, J. Park, S. Kim, I. Cho, H.-H. Yang, M. Cho, S. Mousavi, K. H. Choi, I. Park, Micropatterning of metal oxide nanofibers by electrohydrodynamic (EHD) printing towards highly integrated and multiplexed gas sensor applications, Sens. Actuat. B Chem. 250 (2017) 574–583, https://doi.org/10.1016/j.snb.2017.04.194.
[49] J. Yun, J. Ahn, D. Moon, Y. Choi, I. Park, Joule-heated and suspended silicon nanowire based sensor for low-power and stable hydrogen detection, ACS Appl. Mater. Interfaces. 11 (2019) 42349–42357, https://doi.org/10.1021/acsami.9b15111.
[50] I. Cho, K. Kang, D. Yang, J. Yun, I. Park, Localized liquid-phase synthesis of porous SnO2 nanotubes on MEMS platform for low-power, high performance gas sensors, ACS Appl. Mater. Interfaces. 9 (2017) 27111–27119, https://doi.org/10.1021/acsami.7b04850.
[51] K.I. Chen, B.R. Li, Y.T. Chen, Silicon nanowire field-effect transistor-based biosensors for biomedical diagnosis and cellular recording investigation, Nano Today 6 (2011) 131–154, https://doi.org/10.1016/j.nantod.2011.02.001.
[52] Y. Yokota, K. Ueno, H. Misawa, Essential nanogap effects on surface-enhanced Raman scattering signals from closely spaced gold nanoparticles, Chem. Commun. 47 (2011) 3505–3507, https://doi.org/10.1039/c0cc05320a.
[53] Y.Q. Cao, K. Qin, L. Zhu, X. Qian, X.J. Zhang, D. Wu, A.D. Li, Atomic-Layer-deposition assisted formation of wafer-scale double-layer metal nanoparticles with tunable nanogap for surface-enhanced Raman scattering, Sci. Rep. 7 (2017) 1–8, https://doi.org/10.1038/s41598-017-05533-4.
[54] K.M. Baek, J.M. Kim, J.W. Jeong, S.Y. Lee, Y.S. Jung, sequentially self-assembled rings-in-mesh nanoplasmonic arrays for surface-enhanced Raman spectroscopy, Chem. Mater. 27 (2015) 5007–5013, https://doi.org/10.1021/acs.chemmater.5b01397.
[55] J. Jang, B.G. Hyun, S. Ji, E. Cho, B.W. An, W.H. Cheong, J.-U. Park, Rapid production of large-area, transparent and stretchable electrodes using metal nanofibers as wirelessly operated wearable heaters, NPG Asia Mater. 9 (2017), e432, https://doi.org/10.1038/am.2017.172.
[56] T. Kim, Y.W. Kim, H.S. Lee, H. Kim, W.S. Yang, K.S. Suh, Uniformly interconnected silver-nanowire networks for transparent film heaters, Adv. Funct. Mater. 23 (2013) 1250–1255, https://doi.org/10.1002/adfm.201202013.
[57] S. Choi, J. Park, W. Hyun, J. Kim, J. Kim, Y.B. Lee, C. Song, H.J. Hwang, J.H. Kim, T. Hyeon, D.H. Kim, Stretchable Heater using ligand-exchanged silver nanowire nanocomposite for wearable articular thermotherapy, ACS Nano 9 (2015) 6626–6633, https://doi.org/10.1021/acsnano.5b02790.
[58] D.C. Choo, T.W. Kim, Degradation mechanisms of silver nanowire electrodes under ultraviolet irradiation and heat treatment, Sci. Rep. 7 (2017) 1–12, https://doi.org/10.1038/s41598-017-01843-9.
[59] H.H. Khaligh, L. Xu, A. Khosropour, A. Madeira, M. Romano, C. Pradére, M. Tréguer-Delapierre, L. Servant, M.A. Pope, I.A. Goldthorpe, The joule heating problem in silver nanowire transparent electrodes, Nanotechnology 28 (2017), 425703, https://doi.org/10.1088/1361-6528/aa7f34.
[60] A. Kim, Y. Won, K. Woo, C.H. Kim, J. Moon, Highly transparent low resistance ZnO/Ag nanowire/ZnO composite electrode for thin film solar cells, ACS Nano 7 (2013) 1081–1091, https://doi.org/10.1021/nn305491x.